Journal of Materials Chemistry A



PAPER

View Article Online
View Journal | View Issue



Cite this: J. Mater. Chem. A, 2021, 9, 5702

Received 11th October 2020 Accepted 22nd January 2021

DOI: 10.1039/d0ta09931g

rsc.li/materials-a

Interplay between multiple doping elements in high-voltage LiCoO₂†

Sicheng Song,^a Yiwei Li,^a Kai Yang,^a Zhefeng Chen,^a Jiajie Liu,^a Rui Qi,^a Zhibo Li,^a Changjian Zuo,^a Wenguang Zhao,^a Ni Yang,^a Mingjian Zhang^{*ab} and Feng Pan ^b*ab

Pursing a higher upper cutoff voltage rejuvenates conventional LiCoO₂ (LCO) in the application of high-energy-density Li-ion batteries. Recently, multiple element doping (Q. Liu *et al.*, *Nature Energy*, 2018, 3, 936–943; J. N. Zhang *et al.*, *Nature Energy*, 2019, 4, 594–603) has pushed the upper cutoff voltage to 4.5 and even 4.6 V for achieving a higher energy density. However, reports about the spatial distribution of doping elements in high-voltage LCO are in chaos, and even in conflict. Herein, the interplay between doping elements is clearly revealed by systemic structural and chemical analysis in Ni–Ti–Mg co-doping LCO. When Ni and Ti were employed, they introduced a great extent of poly-crystallization in the original single-crystal LCO, and more importantly, Ti was found to cooperate with Ni to enrich the grain boundary, constructing a stable shell to protect the layered lattice in the bulk. Further introducing Mg induces Ni/Ti to diffuse into the bulk to form the lattice doping, and moreover Mg was segregated at the grain boundary with tiny Ti, delivering a high capacity retention of 90% even after 100 cycles at 4.5 V. These findings answer the previous debate about the distribution of doping elements, and provide more quidance for the design of new doping strategies for high-energy-density LCO cathodes and beyond.

Introduction

Lithium ion batteries (LIBs) with high energy density have nowadays become a vital electrochemical energy storage technology and have been widely utilized in portable mobile devices, transportation, and long-term storage applications.1-6 In the field of portable electronic equipment, LiCoO2 (LCO) still dominates the cathode market because of its simple preparation, high initial coulombic efficiency (>95%) and voltage plateau, and excellent cycling stability (<4.2 V).7-9 Nevertheless, only \sim 50% of Li⁺ is available under the traditional upper cutoff voltage of 4.2 V (vs. Li/Li⁺), which would not meet the requirements of higher energy density for transportation and grid-level energy storage. One feasible method to achieve higher energy density in LCO is to increase the upper cutoff voltage. However, the structural instability in the bulk and at the interface between LCO and other components (e.g., electrolyte, conductive additives 10-14) at high voltages (>4.2 V) leads to the fast deterioration of the electrochemical performance and even safety concerns in LCO-type LIBs.15 Studies have shown that LCO experiences a series of phase transitions from H1 to H2

(\sim 3.9 V, insulator-metal phase transition), M1 (\sim 4.1 V), H3 (\sim 4.2 V, order-disorder transition), M2 (\sim 4.55 V), and O1 (only CoO₂ slab) when charging to high voltages, ^{3,15-22} resulting in a large anisotropic expansion and contraction along the c and a axis. After several cycles, some phase transitions (e.g., H2 to M1, M1 to H3, H3 to M2) become irreversible and lead to severe capacity fading. ²³⁻²⁶ Specially, when charging to 4.2 V, approximately 50% of Li⁺ is removed and the c axis expands significantly, while the a axis changes only slightly. This anisotropic dimensional change induces stress and mechanical fractures within the LCO particles, causing the capacity fading.

Elemental doping is the most widely used method to improve the structural stability of LCO because it can alter the lattice at the atomic scale (including defect concentration, cationic arrangement, charge redistribution and electronic structure) to adjust the physical and chemical properties. Theoretical studies have indicated that TM doping (e.g., Cu, Ni, Mn, Ti, La) and non-TM doping (e.g., Mg, Ca, Al, Si) will lead to an increase in the capacity and charge voltage, 27 respectively, which is beneficial for higher energy density in LIBs. Mg is considered a good doping element in LCO because it is light, nontoxic, cheap, and abundant,28-33 and while Mg doping will slightly reduce the initial discharge capacity, it will significantly improve the cycling performance at voltages higher than 4.2 V.28 Several origins have been proposed for the improved cyclability of Mg-doped LCO, including: (a) the increased electronic conductivity. Tukamoto et al. found that the conductivity at room temperature could be increased by over two orders of

[&]quot;School of Advanced Materials, Peking University, Shenzhen Graduate School, Shenzhen 518055, People's Republic of China. E-mail: panfeng@pkusz.edu.cn; zhangmj@pkusz.edu.cn

^bCenter for Advanced Radiation Source (ChemMatCARS), The University of Chicago, Argonne, Illinois 60439, USA

[†] Electronic supplementary information (ESI) available. See DOI: 10.1039/d0ta09931g

magnitude through the partial substitution of Co³⁺ by Mg²⁺ for hole-creation compensation;²⁸ (b) the pillaring effect.³⁴ Kim et al. suggested that the improvement of the cycling performance by Mg doping is due to the larger lattice parameter and Li slab because of the larger radius of Mg²⁺ than that of Co³⁺, which might help to facilitate the (de)intercalation of Li⁺ and prevent the structure distortion; 29,33 (c) the increased structural reversibility. Tukamoto et al. and other groups found that Mg doping totally suppressed the transition from H2 to M1 and the irreversible transition to H3 around 4.2 V to retain the reversible hexagonal structure and to avoid the unstable monoclinic structure (M1).28-30 On the other hand, Ni and Ti doping have been considered to improve the surficial stability of LCO. Moonsu Yoon et al. revealed that the doped Ni cations moved to the particle surface during cycling, resulting in a cation mixed layer with a thickness of \sim 3 nm at the interface, which could suppress the oxygen release and the structural transition and reduce the interfacial side reactions under high voltages.35 Ti is usually considered for doping on the surface of materials.36,37 Yang et al. concluded that a small amount of Ti doping made the surface smoother and more regular, reduced the polarization during charging and discharging, and endowed LCO with a higher discharge voltage and a smoother discharge plateau.³⁸ Since 2018, more and more high-voltage (4.5 V/4.6 V vs. Li/Li⁺) LCO materials have been reported, 37,39-46 and Mg and Ti doping have been used widely. However, there is a great amount of debate, even conflicts, about the spatial location of these doping elements in these reports. For example, Wang et al. reported the bulk doping of Al and Ti and surface gradient doping of Mg in 4.6 V LCO.40 While, in another study, involving 4.6 V LCO through trace Ti-Mg-Al co-doping, Zhang et al. reported that Mg and Al entered the layered lattice, inhibiting the undesired phase transition at voltages above 4.5 V and that Ti was segregated significantly at the grain boundaries and at the surface, modifying the micro-structure of the particles while stabilizing the surface oxygen at high voltages.37 Based on these conflicting results, we suspect that there must be an interplay between these different doping elements, which governs their distribu-

In this work, we chose three elements, namely Ni, Ti and Mg, to study the interplay between the doping elements in highvoltage LCO. As expected, elemental co-doping significantly improved the structural reversibility and surficial stability of LCO, delivering a high capacity retention of 90% after 100 cycles at 1C (175 mA g⁻¹) while working at a cutoff voltage as high as 4.5 V (vs. Li/Li⁺). Systemic structural and chemical analyses, including X-ray diffraction (XRD), scanning electron microscopy (SEM), focused ion beam (FIB), high-resolution transmission electron microscopy (HRTEM) coupling with energy dispersive spectrometry (EDS), X-ray photoelectron spectroscopy (XPS), etc. were performed. The poly-crystallization effect of elemental doping is clearly demonstrated. Furthermore, the spatial distribution of Ni, Ti, Mg, especially the interplay between them, is also depicted here for the first time, which provides more insights into the fundamental mechanism of element doping in high-voltage LCO.

tion in LCO, as well as their protective roles and the extent.

Results and discussion

Doping effect on the high-voltage performance of LCO

Three samples, namely LCO, LiCo_{0.98}Ni_{0.01}Ti_{0.01}O₂ (LCO-NT), and LiCo_{0.97}Ni_{0.01}Ti_{0.01}Mg_{0.01}O₂ (LCO-NTM), were prepared to study the doping effects. Details about the material preparation can be found in the Experimental section. The chemical composition ratios of Co: Ni: Ti and Co: Mg: Ni: Ti in two doped materials were measured by inductively coupled plasma atomic emission spectrometry (ICP-AES), and the results were basically consistent with the designed ratios (Table S1†).

The cycling performance for LCO was performed in the voltage range of 2.7-4.2 V (Fig. S1†), and the high capacity retention (>90% after 50 cycles) confirmed it as a good baseline. Then the electrochemical performances of LCO, LCO-NT, and LCO-NTM were tested and compared at a high upper cutoff voltage of 4.5 V in the half-cell configuration. As shown in Fig. 1a, LCO-NT and LCO-NTM showed larger initial discharge capacities (184.7 and 180.2 mA h g^{-1} , respectively) than bare LCO (173.4 mA h g^{-1}) at the current density of 0.1C (1C = 175 mA g⁻¹). Notably, the charge curve of LCO-NTM became smooth while bumps occurred at around 4.2 V in the curves of LCO and LCO-NT. This hints that the phase transition involving the unstable monoclinic intermediate (M1 phase, marked by the dotted circle) was greatly suppressed after Mg doping. This could be further confirmed in the dQ/dV curves (Fig. 1b, dotted circles). Two main distinct phase transitions occurred at approximately 4.1 (H2/M1) and 4.2 V (M1/H3), which were

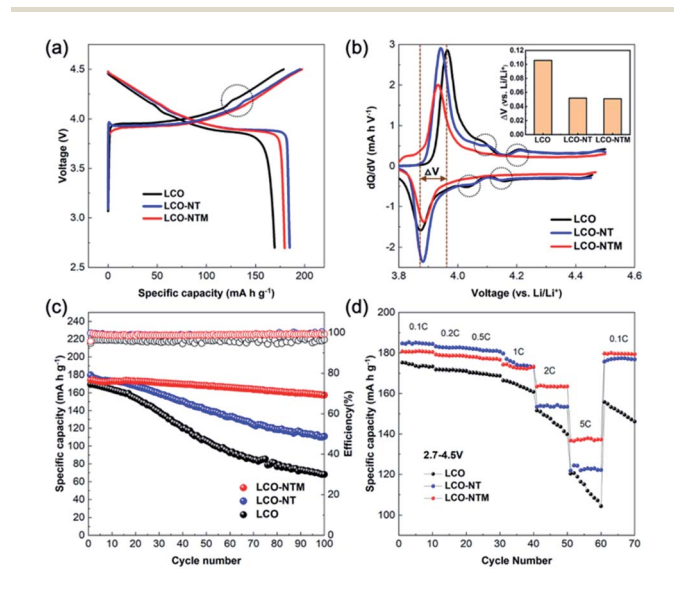


Fig. 1 Electrochemical characterization of LCO and co-doped LCO. (a) First charge/discharge voltage profiles of LCO, LCO-NT, and LCO-NTM in the initial cycle at 0.1C and in the voltage range of 2.7–4.5 V (vs. Li/Li⁺). The phase transition is highlighted by the dotted circle. (b) Corresponding dQ/dV curves of LCO, LCO-NT, and LCO-NTM derived from the voltage profiles in (a). The dashed circles in the profile indicate two distinct phase transitions, respectively. The inset shows the differences of the oxidization peak position and the reduction peak position (denoted as ΔV) for three samples. (c) The cycling performance of three samples at 1C. (d) Rate performance comparison for three samples.

associated with the order–disorder transition near Li $_{0.5}$ CoO $_2$. Such phase-transition peaks totally disappeared for LCO–NTM, indicating that the order–disorder transition had been suppressed or eliminated. In addition, the polarization can be simply evaluated by the difference of the oxidization peak position and the reduction peak position (denoted as ΔV). As shown in the inset of Fig. 1b, the ΔV value was nearly cut in half after elemental doping for both doped samples (0.106, 0.0518, and 0.0508 V for LCO–NT, and LCO–NTM, respectively), indicating that the polarization was greatly reduced by Ni, Ti, and Mg doping. This is another reason for the higher capacity after elemental doping in the same voltage region. A similar phenomenon was also be confirmed by the cyclic voltammetry (CV) curves in Fig. S2d.†

The cycling stability is compared in Fig. 1c. Bare LCO suffered a rapid capacity decay in 100 cycles with a low capacity retention of 40.3% (from 169.5 to 68.3 mA h g^{-1}) at 1C. In contrast, the two co-doped cathodes showed greatly improved cycling stability. LCO-NT exhibited a capacity retention of 61.5% (from 179.7 to 100.9 mA h g^{-1}) after 100 cycles and remarkably, LCO-NTM delivered a very high capacity retention of 90.2% (from 174.2 to 157.2 mA h g^{-1}) after 100 cycles. The much smaller impedance of LCO-NT and LCO-NTM after 100 cycles were consistent with their superior cycling performance (Fig. S3†). In addition, the rate capability was also greatly enhanced in LCO-NT and LCO-NTM. Especially, the latter showed a specific capacity of up to 137.8 mA h g^{-1} even at a high current density of 5C (Fig. 1d), which could be related with the poly-crystallization effect (depicted below). In addition, the electrochemical performance at the higher voltage of 4.6 V were also compared, showing the same trend (Fig. S2†). In other words, an improvement in the electrochemical performances of LCO at high voltages was successfully achieved through Mg/Ni/ Ti co-doping.

Impact of elemental doping on the bulk structure and morphology

We first investigated the impact of elemental doping on the layered lattice in LCO. As shown in Fig. 2a, the crystal structure of LCO can be described as an alternate stacking of Li layers and transition metal layers composed of edge-sharing CoO6 octahedra. The unit cell contained three Li slabs and three Co slabs. When Ni, Ti and Mg were introduced into the layered lattice, they were assumed to take up the Co sites (Fig. 2b) according to previous reports. 28,29,35,38 As shown in Fig. 2c, the XRD patterns of the three samples are similar, indicating the retainment of the layered phase after Ni, Ti and Mg doping. Rietveld refinements were performed to further analyze the detailed structural changes by elemental doping, and the results are presented in Fig. S4a-c and Table S2.† As shown in Fig. 2d, a large increase in lattice parameter c and a decrease in parameter a were found after Ni/Ti doping. Subsequent Mg doping increased parameter c a little, and further decreased a to a similar extent as Ni/Ti doping. This seems abnormal considering the larger radius of Mg^{2+} (0.72 Å) than Ni^{3+} (0.56 Å), Ti^{4+} (0.605 Å) and Co^{3+} (0.545 Å). The change of parameter c can be divided into the

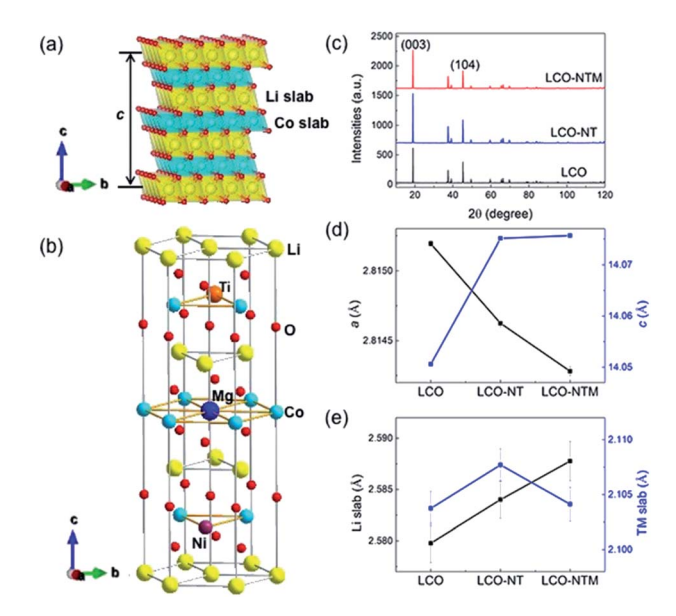


Fig. 2 Impact of elemental doping on the layered structure of LCO. (a) Layered structure of LCO. (b) Schematic lattice structure of LCO–NTM assuming the lattice doping of Ni/Ti/Mg. (c) Normalized XRD patterns of LCO, LCO–NT, and LCO–NTM based on the (003) peak intensity. (d) Comparison of the lattice parameters a and c for the three samples based on Rietveld refinements. (e) Comparison of the Li slab and TM slab for the three samples.

changes of the Li slab and TM slab. As shown in Fig. 2e, the Li slab and TM slab in LCO–NT both increased slightly, leading to a large increase in parameter c. After Mg doping, the TM slab decreased while the Li slab increased, which is generally considered beneficial for Li † (de)intercalation. All these changes in structural parameters should be related with the distribution of doping elements (in the layered lattice or at the surface), and also the interplay between them.

To further compare the morphology, SEM images were recorded. As shown in Fig. 3a-c and S4d-f,† LCO, LCO-NT and LCO-NTM were all made up of 10-15 micrometre secondary particles. Differently, the secondary particle of bare LCO was composed of micrometre-level single crystals sized 2-6 micrometres, while the secondary particles of LCO-NT and LCO-NTM were composed of much smaller primary particles of around several hundred nanometres. To further confirm this phenomenon, focused ion beam (FIB) was used to cut the secondary particles in half, and the ion-induced secondary electron (ISE) images of the cross sections for three samples are compared in Fig. 3d-f. It is clear that the doped materials contained much smaller and compactly stacked nano-crystals, which is consistent with the previous report.37 The specific surface areas of LCO-NT and LCO-NTM were much smaller than that of bare LCO (Table S3†), and close to the estimated value of an ideal single crystal (see the Experimental section), which further confirmed the atomic-level fusion between the primary grains. Such compact stacking can hinder the infiltration of the electrolyte into the secondary particle, and decrease the side reactions related to the electrolyte. Such polycrystallization by elemental doping can introduce lots of grain

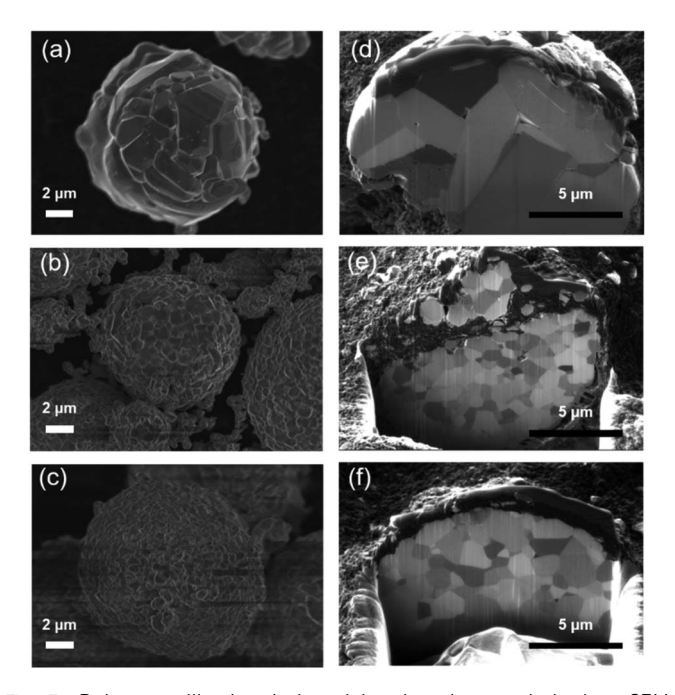


Fig. 3 Poly-crystallization induced by the elemental doping. SEM images of LCO (a), LCO-NT (b) and LCO-NTM (c). Ion-induced secondary electron (ISE) images of the cross-section for LCO (d) LCO-NT (e) and LCO-NTM (f). The cross-section samples were prepared by

boundaries with a modified electronic structure and electric property by elemental enrichment (demonstrated as below), 47-49 which may explain the better rate performance above in the two doped LCO samples. This phenomenon gives us a new understanding of the mechanism beneath elemental doping, which is discussed below.

Distribution of doping elements and the interplay between them

To explain the abnormal structural changes and the improved electrochemistry above, the distribution of doping elements must be illustrated. We focus on two regions: (1) the nearsurface region; (2) the grain boundary region.

As shown in Fig. S5,† TEM images at the near-surface region for LCO, LCO-NT and LCO-NTM were recorded. There was a spinel phase with a thickness of around 10 nm at the surface of LCO (Fig. S5a†), which hinted at a serious Li/O loss at the particle surface. This may be related with the high calcination temperature and the long holding time during synthesis, and may induce the formation of surficial Li₂CO₃.50 This was confirmed by the O 1s and C 1s XPS spectra in Fig. S6 and S7.† In contrast, the doped materials, LCO-NT and LCO-NTM raw materials had clear layered structures under the same synthesis conditions (Fig. S5b and c†), demonstrating the suppression of Li/O loss and thus the subsequent lesser amount of Li₂CO₃ surficial residue during high temperature calcination. TEM-EDX mapping in Fig. S5e† shows that LCO-NT exhibited a uniform distribution of Co, Ni and Ti. Similarly, LCO-NTM also exhibited a uniform elemental distribution of Co, Ni, Ti and Mg (Fig. S5f†). In brief, although the two doped materials had cleaner surfaces than LCO, the elemental distribution was overall uniform at the surface for all three samples.

We went further to check the elemental distribution at the grain boundaries for three samples. As shown in Fig. 4, they all showed a highly continuous and dense grain boundary structure. It is worth noting that LCO-NT had obvious Li/TM antisites at the grain boundary (inset of Fig. 4b), leading to bigger (003) interplanar spacing, but there was no such phenomenon at the grain boundary of LCO-NTM (inset of Fig. 4c). This was also consistent with the refined XRD results (Table S2†). TEM-EDX mapping revealed that Co was uniformly distributed at the grain boundary for LCO (Fig. 4d). After Ni/Ti doping, the grain boundary was enriched with Ni and Ti elements (Fig. 4e), while the content of Co element on the boundary was less than that inside the crystal. To quantitatively analyze the content of Ni and Ti at the grain boundary, line scanning was performed and the results are shown in Fig. S8a and b.† It is clear that the local contents of Ni and Ti relative to Co reached the maximum value of about 10%, respectively, at the grain boundary. Single elemental doping using Ni, Ti or Mg has been widely reported. Ni and Mg doping into LCO is always bulk doping and uniform.35,51 In contrast, Ti always exhibits surface doping due to its poor migration ability.37,38,52 Therefore, it was interesting to observe the cooperative segregation of Ni and Ti at the grain boundary here. The mechanism can be attributed to the charge compensation, since Ti4+ and Ni2+ have an average valence of +3, equal to that of Co³⁺ in the bulk. More interesting, when

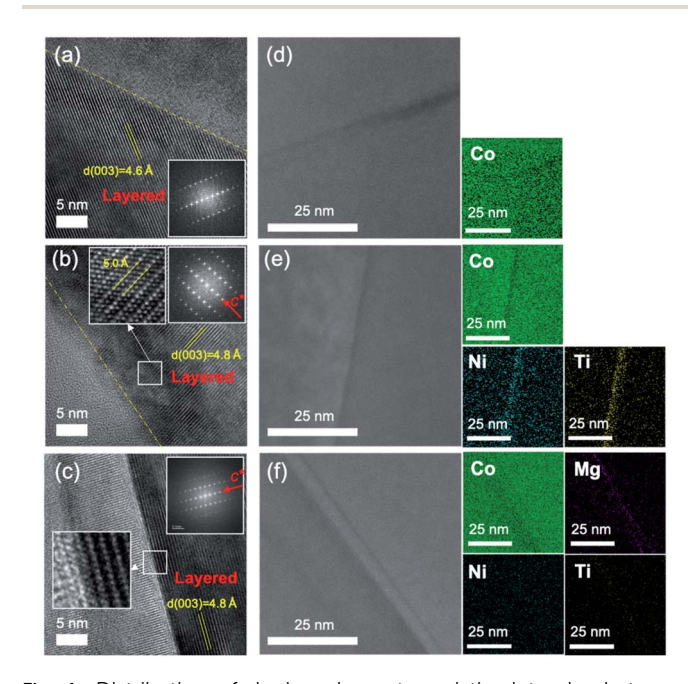


Fig. 4 Distribution of doping elements and the interplay between them at the grain boundary. HRTEM images at the grain boundary of LCO (a), LCO-NT (b) and LCO-NTM (c). The dashed lines are used to mark the locations of the grain boundaries. The enlarged TEM images and selected region FFT maps in the insets in (b) and (c) are used to compare Li/TM anti-sites at the grain boundary. TEM-EDX mapping at the grain boundary of LCO (d), LCO-NT (e) and LCO-NTM (f).

further introducing Mg (Fig. 4f), the grain boundary of LCO–NTM was enriched with a large amount of Mg and tiny Ti, while the Ni element was uniformly distributed in the bulk. As shown in Fig. S8c and d,† the EDX line scanning at the grain boundary indicated that the local contents of Mg and Ti reached about 15% and 5%, respectively. From these results, we can deduce that Mg could help Ni and Ti diffuse into the layered lattice, leaving itself segregated at the grain boundary. This mechanism can be explained by the theoretical calculations of formation energy as below.

Such unique elemental enrichment and interplay at the grain boundary can also be used to explain the polycrystallization observed above. Li $^{+}$ ions and O $^{2-}$ ions can easily migrate into the interior of $\rm Co_3O_4$ crystals at high temperature, which is conducive to the growth of micrometre-level crystals; while the doping elements (Ni, Ti, Mg) have a weaker mobility, especially Ti, due to the strong Ti–O covalent bond. The enrichment at the grain boundary slows down the migration rate of Li $^{+}$ ions and O $^{2-}$ ions into the interior, and hinders the growth of primary particles. As shown in Fig. 3e and f, the lower Ti enrichment at the grain boundary of LCO–NTM compared to LCO–NT leads to a bigger grain size (1–3 μ m) than that of LCO–NT (around 1 μ m). This confirms the critical role of Ti surface doping in the poly-crystallization of LCO.

Structural/chemical stability at the surface and at the grain boundary

To confirm the structural stability due to elemental doping, the local structure and elemental distribution for the three samples were also investigated by HRTEM and TEM-EDX after long-term cycling.

The HRTEM images at the particle surface after 100 cycles as well as the corresponding EDX mapping are shown in Fig. S9.† It is clear that the shell of LCO (Fig. S9a†) was transformed to the rock-salt phase, while the near-surface region evolved to the spinel phase, demonstrating serious structural degradation due to the Li/O loss. However, LCO–NT and LCO–NTM (Fig. S9b and c†), still kept the well-aligned layered phase at the particle surface. In addition, the O 1s spectra from the XPS results (Fig. S6†) reveal that the surface of the two doped materials contained less carbonate species than that of LCO, and the amount of carbonate at the particle surface after 100 cycles was drastically reduced after co-doping. The presence of more carbonate species at the surface would lead to higher impedance, which is consistent with the poor cyclability of LCO, as shown in Fig. 1c.

The HRTEM images at the grain boundary after 100 cycles as well as the corresponding EDX mapping are shown in Fig. 5. As shown in Fig. 5a, there is a big void between the neighbouring grains, which indicated the boundary was cleaved, and this could be further confirmed by the apparent low Co concentration on the expanded grain boundary with the width of around 80 nm (Fig. 5d). This may be due to the anisotropic lattice expansion/contraction during the repeated charge/discharge cycles. In addition, obvious cracks also occurred at the grain boundary of LCO after 100 cycles, as shown in the ISE images of

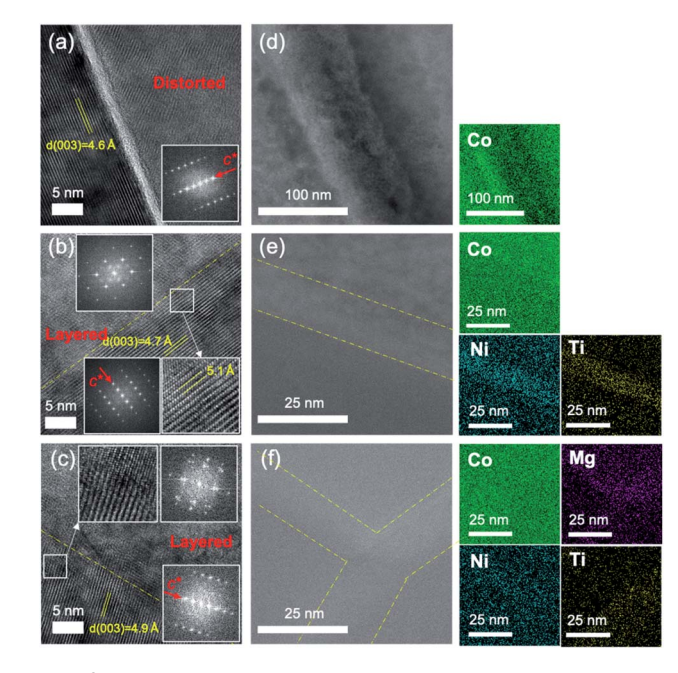


Fig. 5 Structural and chemical stability at the grain boundary. HRTEM images at the grain boundary of LCO (a), LCO-NT (b) and LCO-NTM (c) after 100 cycles at 1C. The enlarged TEM images and selected region FFT maps in the insets in (b) and (c) are used to compare the local structure at the grain boundary. TEM-EDX mapping at the grain boundary of LCO (d), LCO-NT (e) and LCO-NTM (f) after 100 cycles at 1C. The dashed lines are used to mark the locations of the grain boundaries.

the cross-section (Fig. S10†). In contrast, LCO–NT and LCO–NTM still maintained a complete and compact grain boundary structure (Fig. 5b and c), and only slight lattice distortion (with bigger (003) interplanar spacing) is observed in the insets. Corresponding to the TEM-EDX mapping of LCO–NT (Fig. 5e), the boundary was expanded slightly compared with that before cycling (the width changes from 5 to 20 nm). The grain boundary of LCO–NT was still enriched with Ni and Ti elements, and that of LCO–NTM was still enriched with Mg (mainly) and Ti elements as well.

The expansion or compression of layers in different directions during cycling will generate stresses in different directions at the grain boundary, causing expansion and damage to the grain boundary structure till cracks occur. The formation of cracks inside the particles will destroy the integrity of the material's particles and promote more and severe side reactions at high voltages, which will have a serious impact on the cycle stability of the LCO material. Doping elements, including Ni/Ti/Mg, which are enriched on the grain boundary, can efficiently suppress the expansion of the grain boundary and the formation of cracks at the boundary.

Mechanism for the interplay between the doping elements

To validate the effect of Mg on facilitating Ni diffusion into the bulk, we constructed eight structural models for bare LCO, single-element-doped LCO (LCO-N, LCO-T and LCO-M), two-elements-co-doped LCO (LCO-NT, LCO-NM and LCO-TM),

and LCO-NTM, as shown in Fig. 6a and S11,† respectively, for DFT calculations. To reduce the calculation amount, a supercell of 192 atoms was used for LCO (Li₄₈Co₄₈O₉₆), LCO-N (Li₄₈- $Co_{47}NiO_{96}$), LCO-T ($Li_{48}Co_{47}TiO_{96}$) and LCO-M ($Li_{48}Co_{47}$ -MgO₉₆), and a supercell of 96 atoms was applied for LCO-NT (Li₂₄Co₁₂Ni₆Ti₆O₄₈), LCO-NM (Li₂₄Co₁₂Mg₆Ni₆O₄₈), LCO-TM $(Li_{24}Co_{12}Mg_6Ti_6O_{48})$ and LCO-NTM $(Li_{24}Co_6Ni_6Mg_6Ti_6O_{48})$. When adopting the actual doping content (1%) to construct the structural models, a bigger supercell of 384 atoms had to be used for LCO (Li₉₆Co₉₆O₁₉₂), LCO-N (Li₉₆Co₉₅NiO₁₉₂), LCO-T (Li₉₆Co₉₅TiO₁₉₂), LCO-M (Li₉₆Co₉₅MgO₁₉₂), LCO-NT (Li₉₆Co₉₄-NiTiO₁₉₂), LCO-NM (Li₉₆Co₉₄MgNiO₁₉₂), LCO-TM (Li₉₆Co₉₄-MgTiO₁₉₂) and LCO-NTM (Li₉₆Co₉₃NiMgTiO₁₉₂). Since the calculation amount is proportional to the square of the atomic number, the calculation amount for these new models would be 4 times or 16 times that of the corresponding models we used. Four systems were considered: (1) the coexistence of LCO and LCO-NTM; (2) the coexistence of LCO-N and LCO-TM; (3) the coexistence of LCO-T and LCO-NM; (4) the coexistence of LCO-M and LCO-NT. To keep the same atomic number in all four systems, eqn (1) was constructed as below. The corresponding formation energies (E_f) for the eight structural models and four

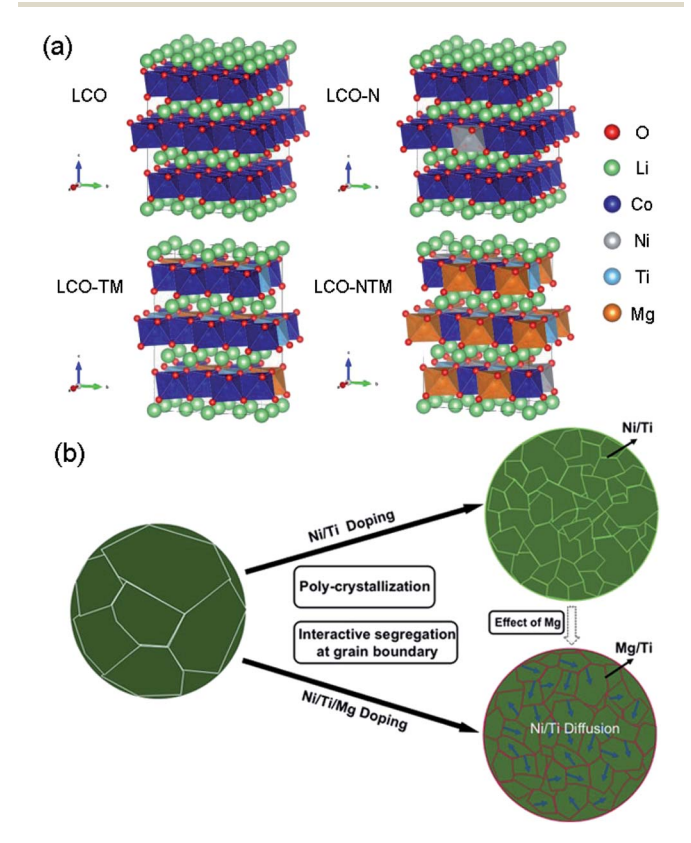


Fig. 6 Theoretical calculations to understand the interplay between the doping elements. (a) Four structure models of LCO, Ti/Mg codoped LCO (LCO-TM), Ni,Ti/Mg co-doped LCO (LCO-NTM) and Nidoped LCO (LCO-N) for DFT calculations of the formation energy to reveal the mechanism of the interplay between Mg and Ni. (b) Schematic illustration to show the effects of multiple elemental doping, including poly-crystallization, elemental segregation and the interplay between doping elements.

systems were calculated based on eqn (2), and the results are shown in Tables S4 and S5 (see details in the ESI).† Among all eight single-phase structural models, LCO-TM had the lowest $E_{\rm f}$ (-3.565 eV per atom), indicating it had the best structural stability. In considering the little doping content (1%) and the segregation of Ni, Ti and Mg, two or more phases would concurrently form at the grain boundaries. Herein, we calculated the $E_{\rm f}$ values for all the two-phase co-existing systems. System (2) had the lowest $E_{\rm f}$ (-3.0312 eV per atom). Therefore, the coexistence of LCO-N and LCO-TM was the most stable from the thermodynamics aspect when introducing Ni, Ti and Mg co-doping. These results successfully explain why Mg can facilitate Ni diffusion into the bulk of LCO.

$$6LCO + LCO-NMT = 6LCO-N + LCO-TM =$$

 $6LCO-T + LCO-NM = 6LCO-M + LCO-NT$ (1)

$$E_{\rm f} = E_{\rm total} - \sum E_{\rm atom} \tag{2}$$

Finally, all the findings are summarized in Fig. 6b. Multiple elemental doping in high-voltage LCO generally induces polycrystallization due to the elemental segregation at the grain boundary, which acts as a protective shell to maintain the structural stability. Moreover, the interplay between doping elements can greatly alter the elemental distribution, and then change the roles of the same doping element.

One other point that needs to be discussed is the polycrystallization induced by elemental doping, which is usually considered as a disadvantage for the structural and cycling stability, considering the greater number of side reactions and poor mechanistic integrity. Actually, the structural instability comes from multiple factors: (1) the larger surface contacting with the electrolyte, leading to severe side reactions; (2) the anisotropic expansion, leading to the cracking of the secondary particles; (3) TM dissolution in the electrolyte.

In this study, these issues were well addressed along with the polycrystallinity. In particular, we found that: (1) the close fusion of primary grains at the atomic level hinders the infiltration of the electrolyte, which blocks the electrolyte at the outmost surface of the secondary particles, thus acting like single crystals; (2) the strong binding of the atomic bonds at the grain boundary effectively mitigates the anisotropic expansion, and prevents the cracking of the secondary particles. This was demonstrated in the TEM images for doping LCO after 100 cycles (Fig. 5). The boundaries were not cracked; (3) similarly, the intact grain boundary slows down the rate of TM dissolution, just as single crystals perform. Furthermore, the elemental enrichment at the grain boundary can effectively decrease the oxygen evolution caused by the oxygen redox at high voltage, greatly enhancing the structural stability.

Furthermore, when we talk about the advantage of single crystals in terms of structural stability, the poor rate performance by the slow Li⁺ insertion/extraction kinetics and the low capacity caused by the larger polarization due to the large particle size have to be considered, although this brings with it a better stability. Another concern is that the content of the Li

source should be finely tuned considering the higher calcination temperature and longer holding time for the growth of micrometre-size single crystals is always accompanied by a greater Li loss.

Experimental

Materials preparation

- (a) Preparation of LiCoO₂. The corresponding amounts of Li $_2$ CO $_3$ and Co $_3$ O $_4$ (molar ratio, Li : Co =1.02:1) were weighed and added into a ball mill jar, with an appropriate amount of absolute ethanol added as a dispersant, followed by ball milling for 6 h. Then, the ball-milled material was dried at 100 °C for 24 h. Finally, the dried material was sintered in a muffle furnace at 1000 °C for 10 h. After cooling, the material was evenly ground, and then subjected to secondary sintering at 900 °C for 10 h. The heating rate was 2 °C min $^{-1}$, and the final product was obtained as a black solid powder.
- (b) Preparation of $LiCo_{0.98}Ni_{0.01}Ti_{0.01}O_2$ (LCO–NT) and $LiCo_{0.97}Mg_{0.01}Ni_{0.01}Ti_{0.01}O_2$ (LCO–NTM). Similarly, Co_3O_4 , $Mg(OH)_2$, $Ni(OH)_2$ and TiO_2 were used as raw materials. The molar ratios were Li:Co:Ni:Ti=1.02:0.98:0.01:0.01 for LCO–NT and Li:Co:Mg:Ni:Ti=1.02:0.97:0.01:0.01:0.01 for LCO–NTM. After sintering, black solid powders were both obtained.

Material characterization

The concentrations of Li, Co, Mg, Ni and Ti in the samples were determined by inductively coupled plasma atomic emission spectroscopy (ICP-AES, JY2000-2). The crystallographic structures of all the cathode materials were investigated by highresolution X-ray diffraction (HRXRD), whose patterns were collected using a Bruker D8-Advance diffractometer with Cu-Ka radiation ($\lambda = 1.5419 \text{ Å}$) at 45 kV and 100 mA. The morphology of the samples was detected by scanning electron microscopy (SEM, ZEISS Supra 55). A focused ion beam (FIB) was used to cut the particles and to detect ISE images of the cross-section. Highresolution transmission electron microscopy (HR-TEM) was performed using a FEI Tecnai G2 F30 TEM microscope. TEM coupled with energy dispersive X-ray spectrometry (EDX) and Xray photoelectron spectroscopy (XPS) were used to detect the elemental distribution of the material particles. The Brunauer-Emmett-Teller (BET) surface areas were measured using the N2 isothermal adsorption method using the ASAP 2020 HD88 surface area analyzer (Micromeritics).

Electrochemical measurements

The cathode electrodes were formed from the mixture of 80 wt% sample powders, 10 wt% acetylene black and 10 wt% poly(vinylidene fluoride) (PVDF) coated on an aluminium foil current collector. The mass loading for all the electrodes was controlled as 1.8 ± 0.2 mg cm $^{-2}$ to ensure the experimental consistency. CR2032 coin-type cells were assembled in an argon-filled glove box and shelved for 12 h before the electrochemical measurement. Lithium foils and polymer membranes were used as the anodes and separators. 1 M LiPF₆ solution with the mixture

solvent of EC, EMC and DMC (1:1:1 by ratio, Tomiyama Pure Chemical Industries, Ltd.) was used as the electrolyte. All the cathode half-cells were charged and discharged on a NEWARE battery test system using a constant current–constant voltage mode at different rates in the voltage range of 2.7–4.5 V and 4.6 V (ν s. Li $^+$ /Li) at 25 °C. The initial five charge–discharge cycles were performed on the assembled cells at a C-rate of 0.1C, and then these were tested with a constant current of 1.0C. The rate capability test was performed at different charge and discharge C-rates of 0.1/0.2/0.5/1.0/2.0/5.0/0.1C for 10 cycles each. Cyclic voltammetry was tested at a sweep speed of 0.05 mV s $^{-1}$ on a model CHI604E electrochemical workstation.

Theoretical calculations

All the calculations were performed using the PWmat code, which is a plane wave pseudopotential package based on density functional theory (DFT) accelerated by the GPU architecture.53,54 The local density approximation (LDA) was chosen as the exchange-correlation potential. The spin = 2 polarization was used in all the calculations. The electron wave functions were expanded by plane waves with cutoff energies of 60 Ryd (816 eV), and the convergence tolerance for the residual force and energy on each atom during structure relaxation were set to 0.02 eV Å^{-1} and 10^{-5} eV , respectively. For k-point integration within the first Brillouin zone, a $2 \times 2 \times 2$ Monkhorst-Pack grid for a supercell of 192 atoms and $4 \times 2 \times 2$ Monkhorst-Pack grid for a supercell of 96 atoms were selected. The Hubbard U (DFT+U) treatment was used on the 3d transition metal to correct the energy and electronic structure of the system. The Uvalues for Co, Ni and Ti were set to 6.7, 5.8 and 4.9 eV, respectively.55,56

Estimation of the specific surface area

We can estimate the specific surface area of an ideal LCO single-crystal sphere with the radius 5 μ m, by using the following equation.

$$S = A/m = (4\pi r^2)/(\rho \times 4/3\pi r^3) = 3/\rho r$$

where S is the specific surface area; A is the surface area of the sphere; m is the mass of the sphere; ρ is the density (the theoretical density of LCO is 5.03 g cm⁻³); and r is the radius of the sphere, 5 μ m. Accordingly, we obtained the specific surface area of 0.12 m² g⁻¹, which was close to the measured values (0.01–0.03 m² g⁻¹).

Conclusions

We used multiple elemental co-doping LCO system to demonstrate the complex behaviours of elemental doping, including the spatial distribution of doping elements and their interplay. Systemic structural and chemical analyses through XRD, SEM, FIB, HRTEM coupled with EDX demonstrated that polycrystallization was generally introduced by doping elemental segregation at the grain boundary, which acted as robust links and buffers between neighbouring primary particles,

suppressing the cleavage and the formation of cracks at the grain boundary, and providing long-term structural stability. Most importantly, the interplay between these doping elements is unveiled for the first time, including the synergistic segregation of Ti and Ni, the induced lattice doping of Ti and Ni by Mg, which can enhance the stability of bulk structure, and the self-segregation of Mg, which can change the distribution of doping elements and the corresponding function of the same doping element. Such interesting interplay gives a reasonable interpretation to the previous chaotic reports about the spatial distribution of doping elements, and may provide beneficial guidance for the design of a multiple elemental doping strategy in high-energy-density layered oxide cathodes and beyond.

Conflicts of interest

There are no conflicts to declare.

Acknowledgements

This work was financially supported by National Key R&D Program of China (2016YFB0700600), Soft Science Research Project of Guangdong Province (No. 2017B030301013), Shenzhen Science and Technology Research Grant (ZDSYS201707281026184).

Notes and references

- 1 J. W. Choi and D. Aurbach, Nat. Rev. Mater., 2016, 1, 16013.
- 2 G. J. Xu, Z. H. Liu, C. J. Zhang, G. L. Cui and L. Q. Chen, J. Mater. Chem. A, 2015, 3, 4092-4123.
- 3 M. Xie, T. Hu, L. Yang and Y. Zhou, RSC Adv., 2016, 6, 63250-63255.
- 4 Y. Y. Jiaxin Zheng and F. Pan, Natl. Sci. Rev., 2020, 7, 242-245.
- 5 Y. K. Ye, J. X. Zheng, T. C. Liu, Y. G. Xiao, C. M. Wang, F. Wang and F. Pan, Acc. Chem. Res., 2019, 52, 2201-2209.
- 6 Y. S. Chen, M. J. Zhang, F. Pan and Y. Ren, Chin. J. Struct. Chem., 2020, 39, 26-30.
- 7 L. L. Wang, B. B. Chen, J. Ma, G. L. Cui and L. Q. Chen, Chem. Soc. Rev., 2018, 47, 6505-6602.
- 8 E. Deiss, A. Wokaun, J. L. Barras, C. Daul and P. Dufek, J. Electrochem. Soc., 1997, 144, 3877-3881.
- 9 A. Manthiram, J. C. Knight, S. T. Myung, S. M. Oh and Y. K. Sun, Adv. Energy Mater., 2016, 6, 1501010.
- 10 J. Janek and W. G. Zeier, Nat. Energy, 2016, 1, 16141.
- 11 A. Manthiram, X. W. Yu and S. F. Wang, Nat. Rev. Mater., 2017, 2, 16103.
- 12 C. W. Sun, J. Liu, Y. D. Gong, D. P. Wilkinson and J. J. Zhang, Nano Energy, 2017, 33, 363-386.
- 13 L. Fan, S. Y. Wei, S. Y. Li, Q. Li and Y. Y. Lu, Adv. Energy Mater., 2018, 8, 1702657.
- 14 Z. H. Gao, H. B. Sun, L. Fu, F. L. Ye, Y. Zhang, W. Luo and Y. H. Huang, Adv. Mater., 2018, 30, 1705702.
- 15 S. Kalluri, M. Yoon, M. Jo, S. Park, S. Myeong, J. Kim, S. X. Dou, Z. P. Guo and J. Cho, Adv. Energy Mater., 2017, 7, 1601507.

- 16 M. Behrens, R. Kiebach, J. Ophey, O. Riemenschneider and W. Bensch, Chem.-Eur. J., 2006, 12, 6348-6355.
- 17 S. H. Min, M. R. Jo, S. Y. Choi, Y. I. Kim and Y. M. Kang, Adv. Energy Mater., 2016, 6, 1501717.
- 18 J. H. Shim, J. M. Han, J. H. Lee and S. Lee, ACS Appl. Mater. Interfaces, 2016, 8, 12205-12210.
- 19 C. A. Marianetti, G. Kotliar and G. Ceder, Nat. Mater., 2004, 3, 627-631.
- 20 X. Lu, Y. Sun, Z. L. Jian, X. Q. He, L. Gu, Y. S. Hu, H. Li, Z. X. Wang, W. Chen, X. F. Duan, L. Q. Chen, J. Maier, S. Tsukimoto and Y. Ikuhara, Nano Lett., 2012, 12, 6192-
- 21 T. Mizokawa, Y. Wakisaka, T. Sudayama, C. Iwai, K. Miyoshi, J. Takeuchi, H. Wadati, D. G. Hawthorn, T. Z. Regier and G. A. Sawatzky, Phys. Rev. Lett., 2013, 111, 056404.
- 22 Y. H. Xu, E. Y. Hu, K. Zhan, X. L. Wang, V. Borzenets, Z. H. Sun, P. Pianetta, X. Q. Yu, Y. J. Liu, X. Q. Yang and H. Li, ACS Energy Lett., 2017, 2, 1240-1245.
- 23 L. J. Liu, L. Q. Chen, X. J. Huang, X. Q. Yang, W. S. Yoon, H. S. Lee and J. McBreen, J. Electrochem. Soc., 2004, 151, A1344-A1351.
- 24 Z. H. Chen and J. R. Dahn, *Electrochim. Acta*, 2004, 49, 1079– 1090.
- 25 G. G. Amatucci, J. M. Tarascon and L. C. Klein, Solid State Ionics, 1996, 83, 167-173.
- 26 R. V. Chebiam, A. M. Kannan, F. Prado and A. Manthiram, Electrochem. Commun., 2001, 3, 624-627.
- 27 G. Ceder, Y. M. Chiang, D. R. Sadoway, M. K. Aydinol, Y. I. Jang and B. Huang, Nature, 1998, 392, 694-696.
- 28 H. Tukamoto and A. R. West, J. Electrochem. Soc., 1997, 144, 3164-3168.
- 29 H. S. Kim, T. K. Ko, B. K. Na, W. I. Cho and B. W. Chao, J. Power Sources, 2004, 138, 232-239.
- 30 M. J. Zou, M. Yoshio, S. Gopukumar and J. Yamaki, Electrochem. Solid-State Lett., 2004, 7, A176-A179.
- 31 F. Nobili, F. Croce, R. Tossici, I. Meschini, P. Reale and R. Marassi, J. Power Sources, 2012, 197, 276-284.
- 32 M. V. Reddy, T. W. Jie, C. J. Jafta, K. I. Ozoemena, M. K. Mathe, A. S. Nair, S. S. Peng, M. S. Idris, G. Balakrishna, F. I. Ezema and B. V. R. Chowdari, Electrochim. Acta, 2014, 128, 192-197.
- 33 H. J. Kim, Y. U. Jeong, J. H. Lee and J. J. Kim, J. Power Sources, 2006, 159, 233-236.
- 34 C. Pouillerie, L. Croguennec, P. Biensan, P. Willmann and C. Delmas, J. Electrochem. Soc., 2000, 147, 2061-2069.
- 35 M. Yoon, Y. Dong, Y. Yoo, S. Myeong, J. Hwang, J. Kim, S. H. Choi, J. Sung, S. J. Kang, J. Li and J. Cho, Adv. Funct. Mater., 2020, 30, 1907903.
- 36 X. B. Hu, M. J. Zhang, M. F. Li, Y. D. Duan, L. Y. Yang, C. Yin, M. Y. Ge, X. H. Xiao, W.-K. Lee, J. Y. P. Ko, K. Amine, Z. H. Chen, Y. M. Zhu, E. Dooryhee, J. M. Bai, F. Pan and F. Wang, Adv. Energy Mater., 2019, 9, 1901915.
- 37 J. N. Zhang, Q. H. Li, C. Y. Ouyang, X. Q. Yu, M. Y. Ge, X. J. Huang, E. Y. Hu, C. Ma, S. F. Li, R. J. Xiao, W. L. Yang, Y. Chu, Y. J. Liu, H. G. Yu, X. Q. Yang, X. J. Huang, L. Q. Chen and H. Li, Nat. Energy, 2019, 4, 594-603.

- 38 X. Yang, J. F. Ni, Y. Y. Huang, J. T. Chen, H. H. Zhou and X. X. Zhang, *Acta Phys.-Chim. Sin.*, 2006, 22, 183–188.
- 39 Q. Liu, X. Su, D. Lei, Y. Qin, J. G. Wen, F. M. Guo, Y. M. A. Wu, Y. C. Rong, R. H. Kou, X. H. Xiao, F. Aguesse, J. Bareno, Y. Ren, W. Q. Lu and Y. X. Li, *Nat. Energy*, 2018, 3, 936–943.
- 40 L. L. Wang, J. Ma, C. Wang, X. R. Yu, R. Liu, F. Jiang, X. W. Sun, A. B. Du, X. H. Zhou and G. L. Cui, Adv. Sci., 2019, 6, 1900355.
- 41 Y. C. Lu, A. N. Mansour, N. Yabuuchi and Y. Shao-Horn, *Chem. Mater.*, 2009, **21**, 4408–4424.
- 42 S. Kalluri, M. Yoon, M. Jo, H. K. Liu, S. X. Dou, J. Cho and Z. P. Guo, Adv. Mater., 2017, 29, 1605807.
- 43 N. T. Wu, Y. Zhang, Y. H. Wei, H. Liu and H. Wu, ACS Appl. Mater. Interfaces, 2016, 8, 25361–25368.
- 44 F. Wang, Y. X. Lin, L. M. Suo, X. L. Fan, T. Gao, C. Y. Yang, F. D. Han, Y. Qi, K. Xu and C. S. Wang, *Energy Environ. Sci.*, 2016, 9, 3666-3673.
- 45 J. Wang, Y. J. Ji, N. Appathurai, J. G. Zhou and Y. Yang, *Chem. Commun.*, 2017, 53, 8581–8584.
- 46 T. Tian, T. W. Zhang, Y. C. Yin, Y. H. Tan, Y. H. Song, L. L. Lu and H. B. Yao, *Nano Lett.*, 2020, **20**, 677–685.

- 47 K. Kawahara, R. Ishikawa, K. Nakayama, T. Higashi, T. Kimura, Y. H. Ikuhara, N. Shibata and Y. Ikuhara, *J. Power Sources*, 2019, **441**, 227187.
- 48 H. Chung and B. Kang, Solid State Ionics, 2014, 263, 125-130.
- 49 S. Kumazaki, Y. Iriyama, K. H. Kim, R. Murugan, K. Tanabe, K. Yamamoto, T. Hirayama and Z. Ogumi, *Electrochem. Commun.*, 2011, 13, 509–512.
- 50 J. Y. L. C. Lin, C. M. Wang and F. Pan, Chin. J. Struct. Chem., 2019, 38, 2015–2019.
- 51 J. Liang, D. H. Wu, M. Hu, Y. Tian, J. P. Wei and Z. Zhou, *Electrochim. Acta*, 2014, **146**, 784–791.
- 52 S. Kim, S. Choi, K. Lee, G. J. Yang, S. S. Lee and Y. Kim, *Phys. Chem. Chem. Phys.*, 2017, **19**, 4104–4113.
- 53 W. L. Jia, J. Y. Fu, Z. Y. Cao, L. Wang, X. B. Chi, W. G. Gao and L. W. Wange, *J. Comput. Phys.*, 2013, **251**, 102–115.
- 54 W. L. Jia, Z. Y. Cao, L. Wang, J. Y. Fu, X. B. Chi, W. G. Gao and L. W. Wang, *Comput. Phys. Commun.*, 2013, **184**, 9–18.
- 55 F. Zhou, M. Cococcioni, C. A. Marianetti, D. Morgan and G. Ceder, *Phys. Rev. B: Condens. Matter Mater. Phys.*, 2004, **70**, 235121.
- 56 G. Y. Gao, K. L. Yaoa, Z. L. Liu, J. Zhang, X. L. Li, J. Q. Zhang and N. Liu, *J. Magn. Magn. Mater.*, 2007, 313, 210–213.